Methane Dry Reforming over Ni/NiO Supported on Ce-, Zr-, and Al-Modified Y$_2$O$_3$ for Hydrogen Production

Zijian Chen, Lei Mao, Xiuzhong Fang *, Xianglan Xu, Junwei Xu and Xiang Wang *

Key Laboratory of Jiangxi Province for Environment and Energy Catalysis, School of Chemistry and Chemical Engineering, Nanchang University, Nanchang 330031, China
* Correspondence: fangxiuzhong@ncu.edu.cn (X.F.); xwang23@ncu.edu.cn (X.W.)

Abstract: In this work, Ce, Zr, and Al are used to promote Y$_2$O$_3$ as supports for Ni/NiO, with the expectation to obtain more efficient catalysts for DRM reaction. XRD and Raman results have testified that all the three cations have been doped into the lattice of Y$_2$O$_3$ to form a solid solution structure, thus obtaining supports with decreased crystallinity and improved surface areas. As a result, all the modified catalysts display evidently improved reaction performance. The Ni–support interaction of the modified catalysts is enhanced in comparison with the unmodified catalyst, thus having improved Ni dispersion. Moreover, the modified catalysts have improved alkalinity, which is beneficial to activate CO$_2$ and enhance the activity. In addition, it is found that all the modified catalysts possess a richer amount of surface active oxygen species (O$_2$$^{\delta-}$ and O$_2$$^-$), which is critical to eliminate carbon depositions. It is believed that the interaction of these factors is responsible for the enhanced DRM performance of the modified catalysts. In situ DRIFTS results have confirmed that the addition of the secondary metals can improve the DRM activity of the catalyst by accelerating the conversion of formate intermediate species.

Keywords: dry reforming of methane; Y$_2$O$_3$ support; secondary metal doping; coking resistance; surface active oxygen species; surface alkaline sites

1. Introduction

The use of fossil energy produces a large amount of CO$_2$, which causes the global greenhouse effect and triggers a series of problems such as glacier melting, sea level rise, and extreme climate [1]. The CO$_2$ molecule has high stability and reaction inertia. To realize added-value CO$_2$ conversion, it is necessary to design a reasonable conversion route. Methane dry reforming (DRM) can convert two greenhouse gases, CH$_4$ and CO$_2$, into syngas. Moreover, the H$_2$/CO ratio in the produced syngas is around 1 [2], which can be directly used as raw materials for the Fischer Tropsch reaction [3]. Therefore, the implementation of the DRM reaction can not only alleviate the energy crisis, but also help to improve the living environment [4], whereas a highly active and effective catalytic system still needs to be developed to industrialize this reaction.

The DRM reaction process usually includes the following reactions:

$$CH_4 + CO_2 \rightarrow 2H_2 + 2CO \quad \Delta H^{\theta}_{298} = +247 \text{ kJ/mol} \tag{1}$$

$$CO_2 + H_2 \rightarrow H_2O + CO \quad \Delta H^{\theta}_{298} = +41 \text{ kJ/mol} \tag{2}$$

$$CH_4 \rightarrow C + 2H_2 \quad \Delta H^{\theta}_{298} = +75 \text{ kJ/mol} \tag{3}$$

$$2CO \rightarrow C + CO_2 \quad \Delta H^{\theta}_{298} = -172 \text{ kJ/mol} \tag{4}$$
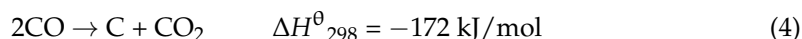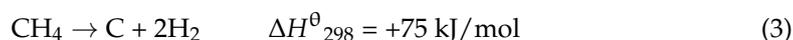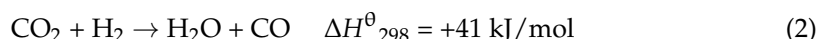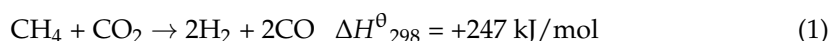
As shown in Equation (1), DRM is a strong endothermic reaction with the formation of 2 mole of more gaseous products [5]. Therefore, it favors high temperature and low pressure in terms of the thermodynamic equilibrium. In the past two decades, Ni-based catalysts

have been widely used in the DRM reaction due to its high initial activity, abundant resources, and relatively low price. However, rapid deactivation of Ni-based catalysts can take place during a DRM process due to severe coke deposition (Equations (3) and (4)) and Ni active site sintering at elevated temperatures. Therefore, it is very important to design and develop a high-efficiency DRM catalyst, which can tolerate high temperature and prevent coke deposition. Up until now, many efforts have been devoted to promote the DRM performance of Ni-based catalysts, for instance: (1) choosing a suitable support to enhance the Ni–support interaction [6]; (2) tuning the surface-acid–base properties and oxygen species by doping with a secondary metal [7]; (3) optimizing the synthesis method to obtain highly dispersed Ni active species [8].

Yttrium oxide, a rare earth oxide, has excellent chemical and thermal durability, which has been employed as catalysts, catalyst supports, or promoters for various reactions [9]. Compared with the acidic Al_2O_3 support and inert SiO_2 support, the alkaline Y_2O_3 support is more conducive to CO_2 adsorption. The activated CO_2 adsorbed on the catalyst surface will generate more adsorbed oxygen (O_{ads}), hence effectively inhibiting carbon deposition [10]. Takeshi et al. prepared nano-porous Ni/Y_2O_3 catalysts with a one-step dealloying technique, which showed significant anti-coking performance compared with traditional Ni-based catalysts [11]. Fatesh et al. loaded Gd and Ni on an Y_2O_3 support, which displayed significantly improved activity compared with the unmodified Ni/Y_2O_3 catalyst, and an 82.8% H_2 yield can be achieved at 700 °C. It was reported that the addition of a secondary active metal component to a DRM catalyst can prevent active site aggregation and coke formation [12]. Mahadi et al. prepared CeO_2, La_2O_3, Sm_2O_3, and Y_2O_3 doping Co/Al_2O_3 catalysts for DRM and found that the dispersion of Co was improved. The Y_2O_3-doped Co/Al_2O_3 catalyst exhibited the best activity and coking-resistance ability [13]. Wang et al. reported enhancing the Ni–support interaction in Ni/ZrO_2 catalysts through Y doping on ZrO_2, thus improving the activity and stability of DRM reaction [14].

Inspired by these previous works, Ce, Zr, and Al were selected as the secondary metals to dope a Ni/Y_2O_3 catalyst to improve its DRM performance. It is well known that CeO_2 has a good oxygen capacity and strong ability to disperse surface active components [15]; ZrO_2 is a metal oxide possessing acidic, basic, and redox properties, and it is easy to generate surface oxygen vacancies [16]; γ-Al_2O_3 is a porous material with good thermal stability and rich surface acidity [17]. By using multiple characterization techniques, it was found that the doping of these secondary metals can affect the Ni–support interaction, thereby improving the Ni dispersion on the surface [18]. The Ce-modified catalyst exhibits the best catalytic stability and the lowest carbon accumulation degree, which is mainly due to the increase in the quantity of active surface oxygen species and the inhibition of Ni sintering.

2. Results

2.1. XRD and Raman Analysis of the Supports

Figure 1A displays the XRD patterns of the supports. The diffraction peaks of the Y_2O_3 support with 2θ of 20.49°, 29.07°, 33.78°, 35.91°, 39.85°, 43.49°, 48.43°, and 57.38° correspond to (211), (222), (400), (411), (332), (431), (440), and (622) crystallite planes of cubic Y_2O_3 [19]. The ion radius of Y^{3+} in Y_2O_3 is 0.102 nm, and the corresponding radii of Ce^{4+}, Zr^{4+}, and Al^{3+} are 0.097 nm, 0.084 nm, and 0.054 nm. For Ce-, Zr-, and Al-doped Y_2O_3 supports, the diffraction peak is similar to that of pure Y_2O_3 without detectable CeO_2, ZrO_2, and Al_2O_3 signals, respectively. The maximum diffraction peaks at around 29° are extracted and enlarged beside the main figure. It is observed that Ce, Zr, and Al with a smaller ionic radius can cause lattice shrinkage after entering the Y_2O_3 lattice, resulting in a peak shift to higher angles [20,21]. As can be seen from cell parameters of the supports in Table S1, the side length decreases after doping with the secondary cations with smaller ion radius. The above results show that the modified Y_2O_3 solid solution supports are successfully synthesized. Meanwhile, the average crystallite sizes of the modified supports are calculated using the Scherrer formula, which are smaller than that of pure Y_2O_3. It can

be seen that the crystallinity of the modified supports decreases after cation doping to form solid solutions, resulting in an increase in the surface area.
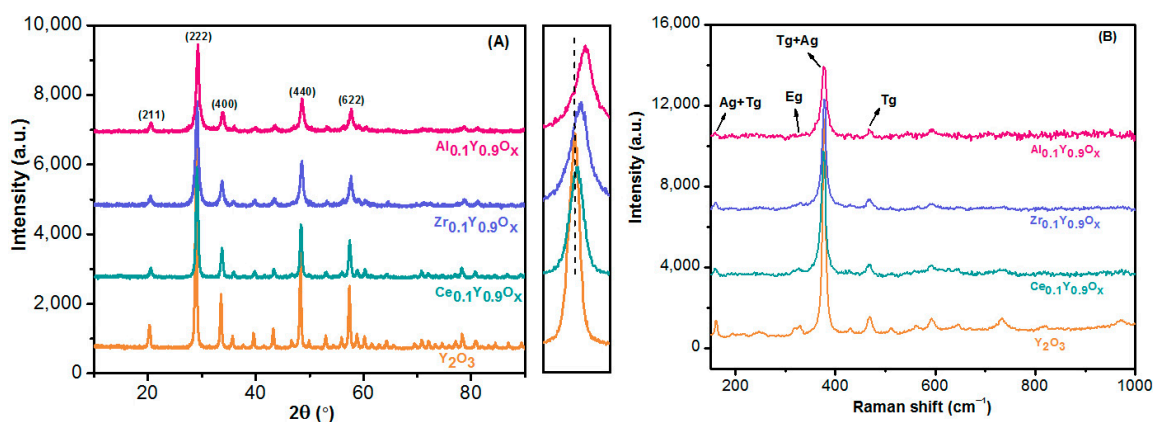

Figure 1. (**A**) XRD patterns and (**B**) Raman spectra of the supports.

The structures of the supports are characterized by Raman spectroscopy in Figure 1B. Several main Raman peaks are observed at 377 cm^{-1}, 330 cm^{-1}, and 469 cm^{-1}, which are attributed to the typical T_g + A_g, E_g, and T_g stretching vibrations modes of the Y_2O_3 phase, respectively [22], and no peaks of other metal oxides are observed. This confirms that all the secondary cations are successfully incorporated into the Y_2O_3 matrix to form a solid solution structure, being well consistent with the XRD results.

2.2. Activity Evaluation

Figure 2 shows the DRM activity test results of the catalysts. All the data are collected after 30 min of stabilization at a corresponding reaction temperature, which can accurately reflect the initial activity at the temperature. As seen from Figure 2A–C, with the increase in the temperature, CH_4 conversion, CO_2 conversion, and H_2 yield increase evidently. From Figure 2D, one can see that the H_2/CO ratio gradually increases with a rise in temperature, which might be ascribable to the reverse water–gas shift reaction (CO_2 + H_2 → CO + H_2O) [23]. The reaction performance of the modified catalysts is generally better than that of the unmodified sample. $5Ni/Al_{0.1}Y_{0.9}O_x$ exhibits the best initial activity, which may be due to its largest surface area (Table S1) and highest Ni dispersion.

To explore the stability of the catalysts, they are tested at 750 °C for 50 h. As exhibited in Figure 3, the unmodified Ni/Y_2O_3 catalyst has low initial activity and poor stability, possibly due to the sintering of Ni active sites and coking. For all the modified catalysts, the $5Ni/Ce_{0.1}Y_{0.9}O_x$ exhibits the most stable CH_4 conversion and H_2/CO ratio, and there is no obvious decrease during the 50 h test, which may be ascribed to the excellent oxygen storage capacity of the CeO_x component. Although $5Ni/Al_{0.1}Y_{0.9}O_x$ and $5Ni/Zr_{0.1}Y_{0.9}O_x$ exhibit a similar initial activity to $5Ni/Ce_{0.1}Y_{0.9}O_x$, more than a 10% drop in CH_4 conversion is detected, indicating that these two catalysts still experience deactivation, but slower than the unmodified Ni/Y_2O_3.

To further investigate the DRM performance of the catalysts, the apparent activation energy of each catalyst is calculated. The CH_4 conversion rates are always maintained below 10% by changing the catalyst amount, and the Arrhenius curves in Figure 3D are drawn with the reaction rates in the range of 450–500 °C. As calculated in Table 1, the unmodified $5Ni/Y_2O_3$ has the largest activation energy of 102.7 KJ·mol^{-1}, while the $5Ni/Al_{0.1}Y_{0.9}O_X$ has the smallest one of 92.8 KJ·mol^{-1}, which is consistent with the reaction performance and surface area results. Meanwhile, the turnover frequency (TOF), Rw, and Rs of CH_4 conversion at 450 °C are specifically calculated for each catalyst. Notably, the TOF is based on Ni loading and dispersion, Rw is normalized by the catalyst mass, and Rs is normalized by the catalyst surface area. Particularly, both TOF and Rs can reflect the intrinsic activity of the catalysts [24]. Obviously, the TOF and Rs rank as $5Ni/Al_{0.1}Y_{0.9}O_x$ > $5Ni/Ce_{0.1}Y_{0.9}O_x$ >

$5Ni/Zr_{0.1}Y_{0.9}O_x > 5Ni/Y_2O_3$, proving that the doping of all the cations can generate more active Ni sites, which enhances the intrinsic activity of the modified catalysts.
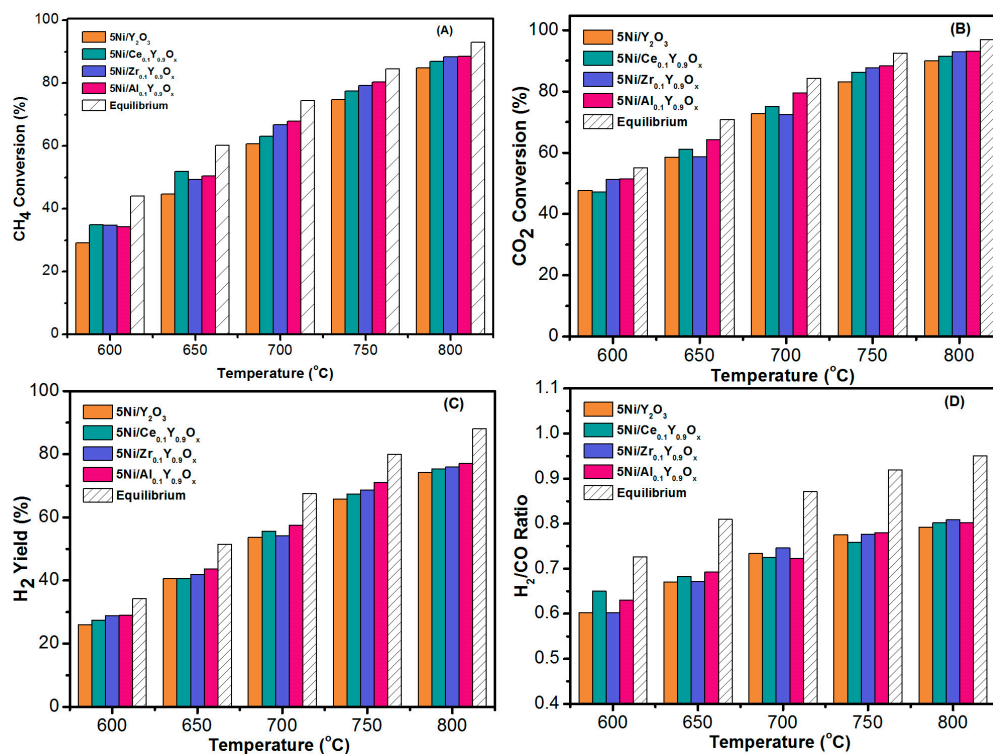
Figure 2. DRM reaction performance of the catalysts: (**A**) CH_4 conversion, (**B**) CO_2 conversion, (**C**) H_2 yield, and (**D**) H_2/CO Ratio.
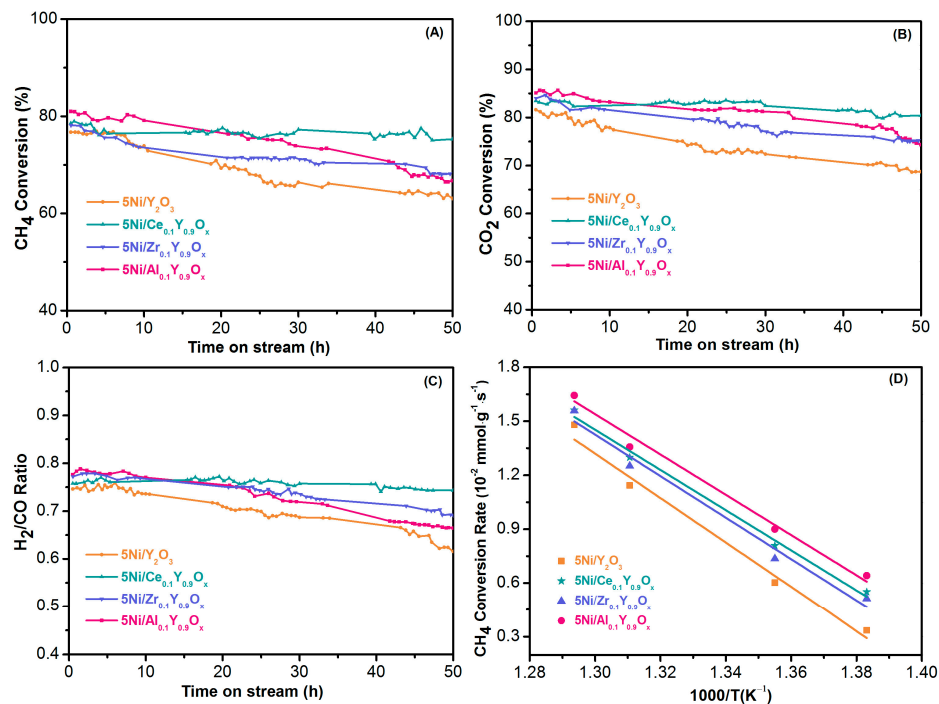
Figure 3. Stability evaluation of the catalysts at 750 °C: (**A**) CH_4 conversion, (**B**) CO_2 conversion, (**C**) H_2/CO Ratio, and (**D**) Arrhenius plots for DRM.

Table 1. DRM kinetics results of the catalysts.

Catalysts	Rw 450 °C $(10^{-3}$ mmol$\cdot$g$^{-1}\cdot$s$^{-1})$ [a]	Rs 450 °C $(10^{-4}$ mmol$\cdot$m$^{-2}\cdot$s$^{-1})$ [b]	TOF 450 °C $(10^{-2}\cdot$s$^{-1})$	Ea $(KJ\cdot mol^{-1})$
$5Ni/Y_2O_3$	3.3	0.8	9.6	102.7
$5Ni/Ce_{0.1}Y_{0.9}O_x$	5.5	1.2	12.7	93.4
$5Ni/Zr_{0.1}Y_{0.9}O_x$	5.2	1.0	11.3	96.0
$5Ni/Al_{0.1}Y_{0.9}O_x$	6.4	1.3	13.6	92.8

[a] Rw: CH_4 conversion rate based on catalyst mass. [b] Rs: CH_4 conversion rate based on catalyst surface area.

2.3. Carbon Deposition on the Spent Catalysts

TGA-DSC and Raman techniques are employed to analyze the coke formation on the spent catalysts after 50 h stability tests. In Figure 4A, the minor weight loss between 100 and 200 °C can be assigned to water desorption, and the major weight loss between 500 and 700 °C can be attributed to the loss of deposited carbon on the spent catalysts, which is accompanied by an evident exothermic peak around 490 °C [25]. As calculated in Table 2, the weight loss of carbon deposition on the unmodified $5Ni/Y_2O_3$ is 11.3%. In contrast, the weight loss of $5Ni/Ce_{0.1}Y_{0.9}O_x$, $5Ni/Zr_{0.1}Y_{0.9}O_x$, and $5Ni/Al_{0.1}Y_{0.9}O_x$ is 3.5%, 4.8%, and 7.4%, respectively, testifying that Ce, Zr, or Al doping can effectively suppress coking of the modified catalysts. The coking rates on the used catalysts are also calculated, which follows the order of $5Ni/Ce_{0.1}Y_{0.9}O_x < 5Ni/Zr_{0.1}Y_{0.9}O_x < 5Ni/Al_{0.1}Y_{0.9}O_x < 5Ni/Y_2O_3$. $5Ni/Ce_{0.1}Y_{0.9}O_x$ displays the slowest coking speed, in good accordance with its most stable reaction performance in all the catalysts.
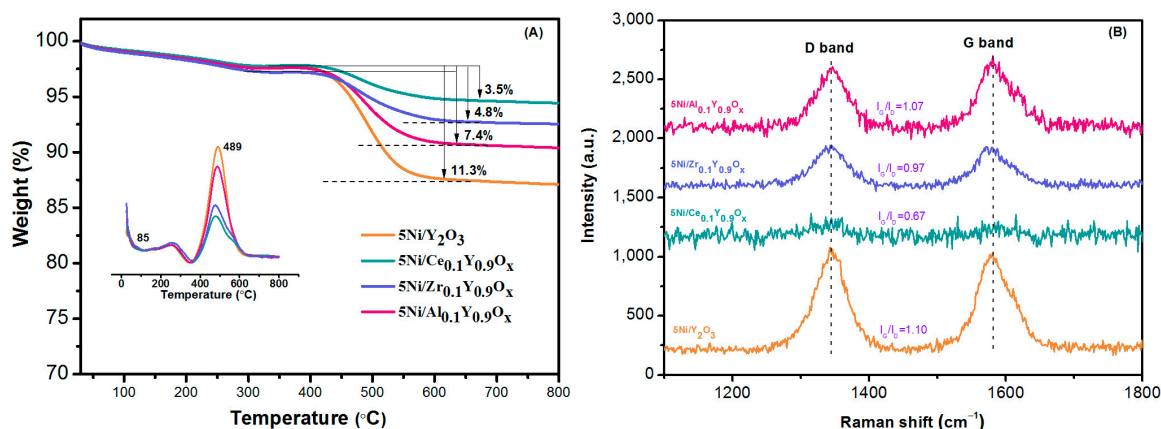
Figure 4. Carbon deposit analysis of the catalysts after 50 h tests at 750 °C for DRM: (**A**) TGA-DSC profiles; (**B**) Raman spectra.

Table 2. Quantified coking results measured by Raman and TGA-DSC.

Catalysts	Weight Loss of Carbon Deposition (%)	Coking Rate (mg$\cdot$g$_{cat}$$^{-1}\cdot$h^{-1}) [a]	I_G/I_D
$5Ni/Y_2O_3$	11.3	2.3	1.10
$5Ni/Ce_{0.1}Y_{0.9}O_x$	3.5	0.7	0.67
$5Ni/Zr_{0.1}Y_{0.9}O_x$	4.8	1.0	0.97
$5Ni/Al_{0.1}Y_{0.9}O_x$	7.4	1.5	1.07

[a] Temperature ranged from 300 °C to 800 °C from TGA.

The Raman spectra are demonstrated in Figure 4B, in which two carbon peaks can be obviously observed. The peak at 1350 cm^{-1} is named the D band corresponding to amorphous carbon deposits, which is easier to remove [26]. The peak at 1580 cm^{-1} is named the G band with respect to graphitized carbon, which is more difficult to eliminate and is usually considered to be a main cause of catalyst deactivation in DRM [27]. The intensity

ratio of the G band to the D band (I_G/I_D) can be used to determine the graphitization degree of coking, hence being calculated in Table 2. The I_G/I_D of the unmodified Ni/Y_2O_3 catalyst is largest, indicating that it has the highest graphitization degree among all the catalysts. The addition of all the secondary metal cations decreases the graphitization degree, as testified by the decreased I_G/I_D values. Notably, $5Ni/Ce_{0.1}Y_{0.9}O_x$ shows the smallest graphitization degree, testifying that most of its carbon deposit is in an amorphous state. Therefore, it is concluded that the Ce doping is the most effective to increase the coking-resistance ability of Ni/Y_2O_3. In brief, both TGA-DSC and Raman results are consistent with each other, which also agrees with the stability test data.

2.4. XRD and N_2-BET of the Freshly Calcined, Reduced, and Spent Catalysts

The XRD patterns of the freshly calcined, reduced, and spent catalysts are presented in Figure 5. Figure 5A shows the XRD results of the fresh catalysts. The typical diffraction peaks of NiO crystallites can be observed along with the initial diffraction peaks belonging to the Y_2O_3 phase, but with varied intensities for the modified and unmodified Ni/Y_2O_3 catalysts [19,28]. The NiO mean crystallite sizes of the catalysts are calculated by the Scherler formula with the NiO (111) peak, and listed in Table 3. $5Ni/Y_2O_3$, the unmodified catalyst with the worst performance, has the largest NiO size of 11.5 nm. The NiO crystallite size decreases, and the surface area increases after metal cation doping.
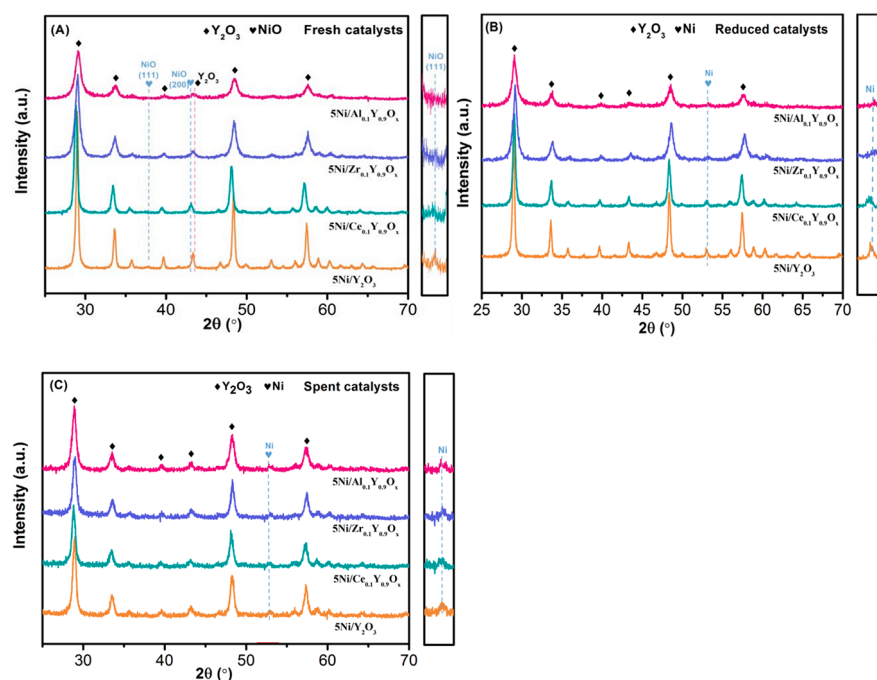

Figure 5. XRD of the (**A**) Fresh, (**B**) Reduced, and (**C**) Spent catalysts.

Table 3. Surface areas and crystallite sizes of the catalysts before and after the reaction.

Catalysts	Fresh Catalysts		Reduced Catalysts		Used Catalysts	
	Surface Area ($m^2 \cdot g^{-1}$) [b]	NiO Crystallite Size (nm) [a]	Surface Area ($m^2 \cdot g^{-1}$)	Ni Crystallite Size (nm)	Surface Area ($m^2 \cdot g^{-1}$)	Ni Crystallite Size (nm)
$5Ni/Y_2O_3$	39.7	11.5	37.9	12.6	33.5	22.5
$5Ni/Ce_{0.1}Y_{0.9}O_x$	43.4	10.3	41.1	11.0	39.5	14.5
$5Ni/Zr_{0.1}Y_{0.9}O_x$	43.8	10.0	42.0	10.9	39.8	15.7
$5Ni/Al_{0.1}Y_{0.9}O_x$	53.1	9.2	51.3	10.2	48.3	17.3

[a] Calculated from XRD; [b] Determined by N_2-BET.

In Figure 5B, all the reduced catalysts present characteristic diffraction peaks of the Ni phase, demonstrating that the original NiO has been fully reduced to metallic Ni. To facilitate comparison, the mean Ni crystallite sizes of the reduced catalysts are also calculated in Table 3. Obviously, $5Ni/Al_{0.1}Y_{0.9}O_x$ has the smallest size of 10.2 nm, corresponding to its highest initial activity among all the catalysts. In addition, $5Ni/Al_{0.1}Y_{0.9}O_x$ has the largest surface area in all the catalysts despite it being freshly calcined, reduced, or used.

Figure 5C demonstrates the XRD patterns of the catalysts after the 50 h stability test. It is observed that the intensities of the metallic Ni phase in the catalysts increase, indicating that the Ni grains aggregate during the long-term DRM tests. As shown in Table 3, the Ni crystallite size of $5Ni/Ce_{0.1}Y_{0.9}O_x$ catalyst increases slowly from 11.0 nm to 14.5 nm after the 50 h reaction, which is slower than the growth rate of Ni grains on the other three catalysts, indicating that the catalysts have the best thermal stability. Therefore, it is inferred that the Ni–support interaction of the $5Ni/Ce_{0.1}Y_{0.9}O_x$ catalyst could be the strongest among all the catalysts. Former studies have shown that the crystallite size of Ni plays a key role for the activity, stability, and anti-coking ability of a DRM catalyst. Usually, a smaller crystallite size relates to better activity, stability, and anti-coking ability [29].

2.5. TEM Analysis of the Ni Distribution over the Fresh Ni/Y_2O_3 Catalysts

TEM and HRTEM tests are carried out to study the morphology and particle size distribution of the catalysts. In Figure 6, all the modified and unmodified Ni/Y_2O_3 catalysts are composed of irregular particles without a special shape. In addition, it is noted that the NiO particle size from TEM is slightly larger than the crystallite size calculated by XRD, indicating that Ni has slight secondary aggregation [30]. The NiO particle sizes calculated by TEM are in the sequence of $5Ni/Y_2O_3 > 5Ni/Ce_{0.1}Y_{0.9}O_x > 5Ni/Zr_{0.1}Y_{0.9}O_x > 5Ni/Al_{0.1}Y_{0.9}O_x$. The result is similar to the crystallite sizes measured by XRD, which confirms that the modification by the secondary metal cations improves the dispersion of the active Ni/NiO component. In addition, HRTEM images show that NiO crystallites are detected, which mainly expose the (200) crystal plane. In addition to this, only Y_2O_3 particles that mainly expose the (222) crystal plane are observed. No other metal oxide components are found. The HRTEM results correspond to the XRD patterns, which further proves the successful synthesis of the solid solution supports, with the Ce^{4+}, Zr^{4+}, and Al^{3+} cations being incorporated into the lattice of cubic Y_2O_3.

2.6. H_2-TPR and XPS Studies of the Freshly Calcined Catalysts

The H_2-TPR technique is employed to investigate the redox behaviors of the supports and the freshly calcined catalysts. As shown in Figure S1, all the supports, either unmodified or modified, do not display any evident reduction peak below 800 °C. This indicates that all the detected peaks on the Ni/Y_2O_3 catalysts in Figure 7 can be ascribed to the reducing of NiO species. The H/Ni atomic ratios in Table 4, which are normalized by NiO contents, are about 2 for all the samples, indicating that Ni species exist predominantly in the form of the Ni^{2+} state.

The low-temperature peak around 350 °C is attributed to the reduction of crystalline NiO grains, which has weak interaction with the support and is easy to reduce. The peak around 400 °C is relatively broad, which could relate to the NiO species having close contact with the support, and has stronger interaction, thus being more difficult to reduce [31]. During the reduction process, this part of NiO can form highly dispersed Ni active species on the surface of the catalysts because of the retarded nucleation process [32]. Based on the quantification results in Table 4, all the modified catalysts possess a larger amount of H_2 consumption of this peak than the unmodified $5Ni/Y_2O_3$, thus obtaining smaller Ni crystallites, as detected by XRD. In more detail, the H_2-TPR results show that NiO and $Ce_{0.1}Y_{0.9}O_x$ have the largest amount of H_2 uptake of this peak, implying that Ni/NiO can be strongly anchored on the $Ce_{0.1}Y_{0.9}O_x$ support surface, thereby obtaining the smallest Ni/NiO crystallite size, which explains its superior stability.
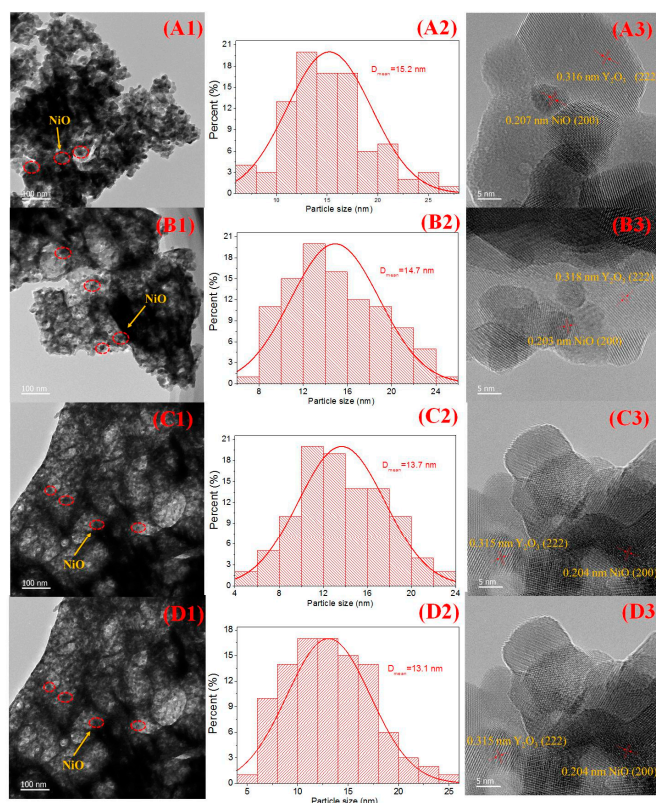
Figure 6. TEM images (**A1,B1,C1,D1**), particle size distribution (**A2,B2,C2,D2**) and HRTEM images (**A3,B3,C3,D3**) of the freshly calcined catalysts. (**A1–A3**) $5Ni/Y_2O_3$, (**B1–B3**) $5Ni/Ce_{0.1}Y_{0.9}O_x$, (**C1–C3**) $5Ni/Zr_{0.1}Y_{0.9}O_x$, (**D1–D3**) $5Ni/Al_{0.1}Y_{0.9}O_x$.
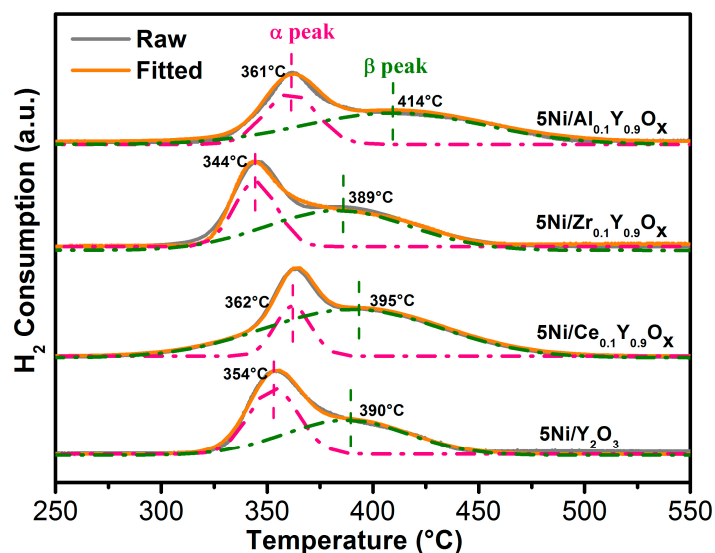

Figure 7. H_2-TPR profiles of the fresh catalysts.

Table 4. Quantified H_2-TPR results of the fresh catalysts.

Catalysts	H_2 Consumption (mmol·g^{-1})			
	α Peak	β Peak	Total	H/Ni
$5Ni/Y_2O_3$	0.37	0.49	0.86	2.0
$5Ni/Ce_{0.1}Y_{0.9}O_x$	0.16	0.71	0.87	2.0
$5Ni/Zr_{0.1}Y_{0.9}O_x$	0.30	0.59	0.89	2.1
$5Ni/Al_{0.1}Y_{0.9}O_x$	0.27	0.60	0.87	2.0

XPS is thus employed to investigate the interaction between NiO and the supports. Figure S2A shows that the peaks at 855.0 eV and 860.8 eV are attributed to Ni $2p_{3/2}$ and Ni $2p_{1/2}$ of Ni^{2+} [33], respectively, in line with the H_2-TPR results. Figure S2B shows that the signals around 157.9 eV and 159.9 eV can be indexed to Y $3d_{5/2}$ and Y $3d_{3/2}$ of Y_2O_3, respectively [34]. With the modification by Ce, Zr, and Al, the Ni 2p peak is shifted to lower binding energies, suggesting the increase in Ni electron density. Considering the charge conservation law, other elements must show a decrease in electron density. As proved in Figure S2B, the binding energies of the two Y 3d peaks shift to a higher value. This finding is consistent with the H_2-TPR results, suggesting that the NiO–support interaction can be regulated and strengthened by the modification of Ce, Zr, and Al cations.

2.7. H_2 Adsorption–Desorption Analysis of the Freshly Reduced Catalysts

H_2 sorption is employed to investigate the Ni dispersion and active Ni surface area with the reduced catalysts. The dispersion of Ni has an important influence on the DRM reactivity, which will affect the activity, stability, and anti-coking ability of a catalyst [35,36]. The Ni contents of the four catalysts are determined by ICP-OES (Table 5), which is the same as the original formulation calculation. The H_2 desorption amount, Ni active surface areas, and Ni dispersion of all reduced catalysts are listed in Table 5, which follow the order of $5Ni/Al_{0.1}Y_{0.9}O_x$ > $5Ni/Zr_{0.1}Y_{0.9}O_x$ > $5Ni/Ce_{0.1}Y_{0.9}O_x$ > $5Ni/Y_2O_3$. Apparently, being consistent with the Ni crystallite sizes measured by XRD, the active metallic Ni surface areas of the modified catalysts are obviously improved by the doping of Ce, Zr, and Al cations to form solid solutions. This explains how all the modified catalysts show better reactivity than the unmodified $5Ni/Y_2O_3$.

Table 5. Ni dispersion and metallic Ni surface areas of the reduced catalysts.

Catalysts	Ni Content (wt.%) [a]	H_2 Desorption ($\mu mol \cdot g^{-1}$)	Ni Surface Area ($m^2 \cdot g_{cat}^{-1}$)	Ni Surface Area ($m^2 \cdot g_{Ni}^{-1}$) [b]	Ni Dispersion (%)
$5Ni/Y_2O_3$	4.98	31.2	1.5	30.9	3.6
$5Ni/Ce_{0.1}Y_{0.9}O_x$	4.97	42.9	2.0	42.3	5.0
$5Ni/Zr_{0.1}Y_{0.9}O_x$	4.97	43.2	2.1	42.8	5.1
$5Ni/Al_{0.1}Y_{0.9}O_x$	4.98	46.8	2.3	46.4	5.5

[a] Ni loading determined by ICP. [b] Based on the cross-sectional area of one surface Ni atom, 8.24×10^{-20} m^2, 0.5% Pt/Al_2O_3(D = 34.5%) as the standard.

2.8. Surface Oxygen Properties of the Catalysts Investigated with XPS and O_2-TPD

The surface oxygen species are investigated by XPS for the catalysts, with the O 1s signals illustrated in Figure 8. By deconvolution, three kinds of oxygen species in different chemical states are obtained for all the catalysts. In detail, the bands around 528.8, 531.0, and 532.8 eV can be assigned to the surface lattice oxygen (O_{latt}), oxygen species related to CO_3^{2-} (O_{carb}), and adsorbed oxygen (O_{ads}), respectively [37]. It is worth noting that a large amount of surface carbonate has been formed on all the catalysts due to the alkalinity of the Y_2O_3 surface. The in situ DRIFTS results in Figure 9 also confirm this, which is discussed further in the related places.

The O_{ads} species is usually considered as an active oxygen species, which can activate the carbon deposition on the catalyst surface during the DRM reaction [38], and eliminate the carbon depositions. Therefore, the relative percentage of O_{ads} is calculated in Table 6. In comparison with the unmodified $5Ni/Y_2O_3$, all the modified catalysts possess obviously increased O_{ads} proportion. This explains the TGA-DSC and Raman results, that all the modified catalysts have better anti-coking ability than the un-modified $5Ni/Y_2O_3$. Among all the modified catalysts, $5Ni/Ce_{0.1}Y_{0.9}O_x$ owns the highest O_{ads} percentage, suggesting that it has a larger quantity of oxygen vacancies than the other two modified catalysts, thus resulting in the best stability and coking-resistance ability [39]. The oxygen adsorption process could be divided into the following three steps, $O_2(ad) \rightarrow O^{2-}(ad) \rightarrow O^-(ad) \rightarrow$

O^{2-} (lattice). The presence of more surface vacancies generally favors the dissociation of gaseous O_2 to generate adsorbed oxygen species (O^{2-} and O^-) [40].
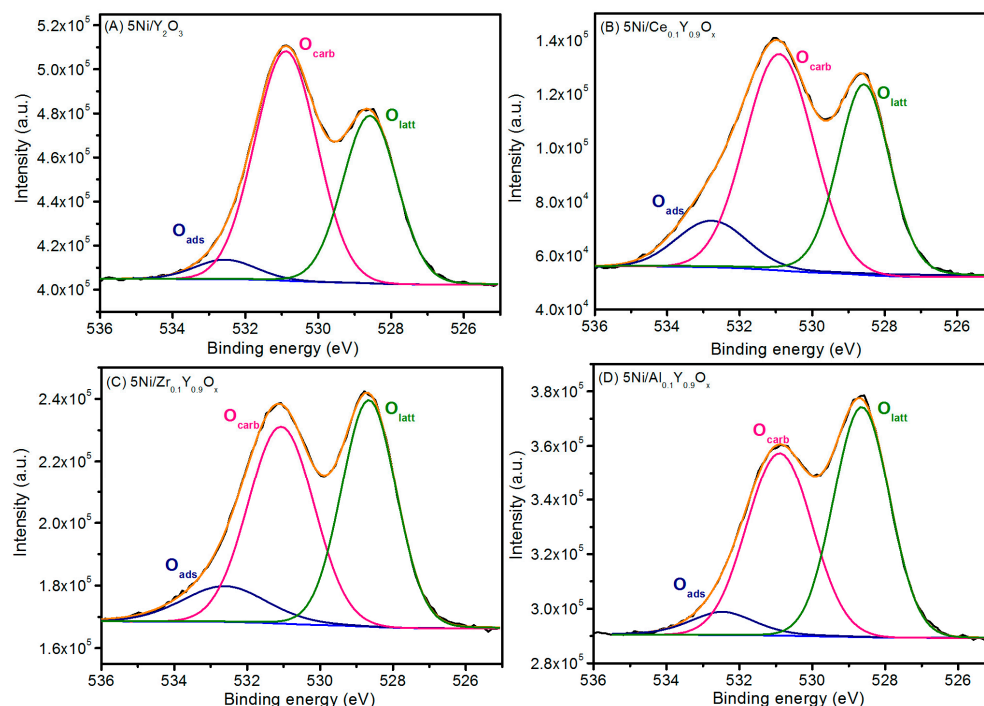

Figure 8. XPS O 1s spectra of the fresh catalysts. (**A**) $5Ni/Y_2O_3$, (**B**) $5Ni/Ce_{0.1}Y_{0.9}O_x$, (**C**) $5Ni/Zr_{0.1}Y_{0.9}O_x$, (**D**) $5Ni/Al_{0.1}Y_{0.9}O_x$.
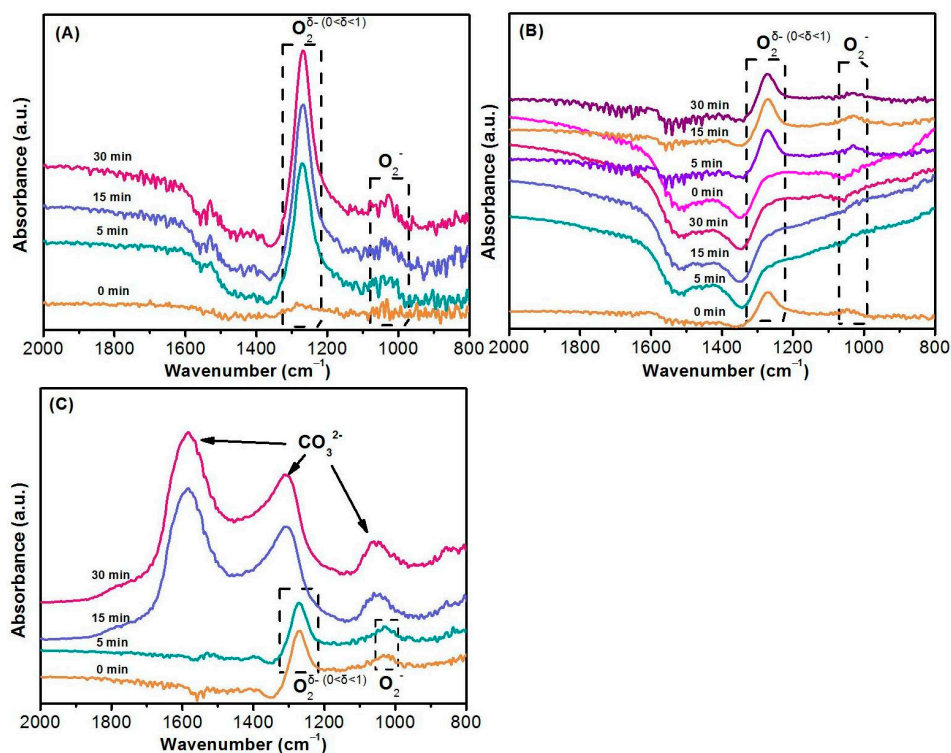

Figure 9. In situ DRIFTS spectra of $5Ni/Ce_{0.1}Y_{0.9}O_x$ at 300 °C: (**A**) Treated in 10% O_2/Ar flow; (**B**) Switched to 5% H_2/Ar flow then changed to 10% O_2/Ar flow; (**C**) Treated in 10% CO_2/Ar after being treated in 5% O_2/Ar flow for 30 min.

The oxygen species and their states on the catalysts are further investigated by O_2-TPD, with the profiles shown in Figure S3. In O_2-TPD curves, the desorption peaks below 300 °C, at 300–550 °C, and above 500 °C could, respectively, be classified as weakly adsorbed oxygen, strongly adsorbed oxygen, and surface lattice oxygen [41]. According to the temperature, the desorption peaks are divided into α and β regions, which are quantitatively analyzed in Table 6. Similar to the XPS results, all the modified catalysts possess a larger amount of total active oxygen species than the unmodified $5Ni/Y_2O_3$. Again, the catalyst modified by Ce owns the largest amount of active oxygen species, which is well consistent with its best reaction stability and anti-coking ability. Indeed, this proves further that the amount of active oxygen species has a tight relationship with the stability and anti-coking performance of a DRM catalyst.

Table 6. Surface oxygen characteristics of the catalysts identified by XPS and O_2-TPD.

Catalysts	O 1s, B.E./FWHM (eV)			$O_{ads}/(O_{ads} + O_{latt} + O_{carb})$ (%)	O_2 Desorption Amount (μmol·g^{-1})		
	O_{ads}	O_{carb}	O_{latt}		α Peak	β Peak	Total
$5Ni/Y_2O_3$	532.6/1.8	530.9/2.0	528.6/1.9	6.6	10.0	10.4	20.4
$5Ni/Ce_{0.1}Y_{0.9}O_x$	532.7/2.0	530.9/2.1	528.7/1.8	12.0	7.3	20.0	27.3
$5Ni/Zr_{0.1}Y_{0.9}O_x$	532.8/2.0	531.0/2.0	528.6/1.8	10.1	10.7	14.2	24.9
$5Ni/Al_{0.1}Y_{0.9}O_x$	532.8/1.9	531.1/2.0	528.8/1.8	7.7	10.3	11.8	22.1

2.9. Identifying the Surface Oxygen Species with In Situ DRIFTS

To distinguish the surface oxygen species, $5Ni/Ce_{0.1}Y_{0.9}O_x$ with the best stability and anti-coking performance is subjected to in situ DRIFTS tests after reduction. First, the sample is pretreated with 99.99% Ar at a flow rate of 30 mL·min^{-1} at 500 °C for 1 h to eliminate surface impurities and physically adsorbed oxygen species. Subsequently, the temperature is lowered to 300 °C and 10% O_2/Ar is introduced. As shown in Figure 9A, the intensity of the peaks at 1270 cm^{-1} and 1030 cm^{-1} gradually increases with time extension, which are attributed to the vibrational peaks of the active oxygen species $O_2^{\delta-\ (0<\delta<1)}$ and O_2^-, respectively [42,43]. This indicates that gaseous O_2 can be adsorbed on the surface oxygen vacancies to form active oxygen species.

Afterward, the atmosphere is switched to 10% H_2/Ar. Figure 9B shows that the peaks of the active oxygen species gradually weaken, and disappear after 5 min. Then, the gas atmosphere is switched back to 10% O_2/Ar flow, and it is found that those active oxygen species recover.

After the oxygen adsorption is saturated, the gas atmosphere is changed to 10% CO_2/Ar flow. Figure 9C shows that the peaks of the active oxygen species gradually weaken and vanish, accompanying the generation of surface CO_3^{2-} species. This has demonstrated that the active oxygen species can react with CO_2 to produce carbonate. Therefore, it is postulated that $O_2^{\delta-\ (0<\delta<1)}$ and O_2^- are the active oxygen sites on catalysts, which could be important for the DRM reaction.

2.10. CO₂-TPD of the Reduced Catalysts

The amount of surface alkaline centers also plays a crucial role in DRM reaction. According to the previous literatures, the surface alkaline sites can adsorb and activate CO_2 molecules to generate reactive intermediates and surface oxygen species [44]. The adsorbed oxygen species is active to remove the initially formed carbon-deposition in time, which is favorable for DRM reaction. Therefore, CO_2-TPD is used to characterize the surface alkalinity of the pre-reduced catalysts. Figure 10 shows that all the catalysts have three alkaline peaks with different intensities. It was reported that the peak below 250 °C is attributed to the desorption of CO_2 on the weak alkaline sites. Due to its easy desorption, this part of adsorbed CO_2 could have limited contribution to the reaction [45]. The peak between 250 and 500 °C is attributed to the desorption of CO_2 on the moderate alkaline sites, which could contribute significantly to the reaction [46]. In fact, the CO_2 in the DRM reaction could mainly adsorb on this part of moderate alkaline sites. However, the peak

above 500 °C is attributed to the desorption of CO_2 on the strong alkaline sites, possibly due to the decomposition of carbonate. Due to its difficulty to be desorbed, this part of adsorbed CO_2 could also have little contribution to the reaction. The quantified results in Table 7 have testified that all the modified catalysts possess more moderate alkaline sites than the unmodified $5Ni/Y_2O_3$, which is consistent with their improved DRM performance. Notably, $5Ni/Ce_{0.1}Y_{0.9}O_x$ has the largest amount of CO_2 desorption, especially the largest amount of CO_2 on the moderate alkaline sites, proving that it has the best ability to adsorb and activate CO_2 molecules.
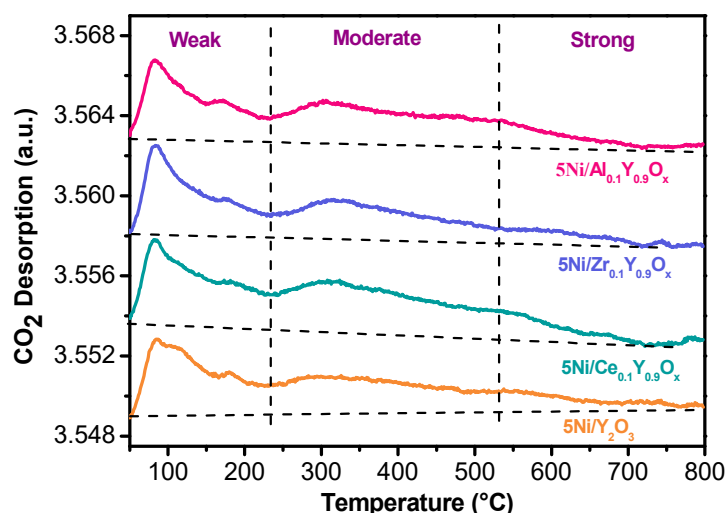

Figure 10. CO_2-TPD profiles of the reduced catalysts.

Table 7. CO_2 desorption amount of the reduced catalysts.

Catalysts	CO_2 Desorption ($\mu mol \cdot g^{-1}$)			
	Weak	Moderate	Strong	Total
$5Ni/Y_2O_3$	17.1	14.8	5.0	36.9
$5Ni/Ce_{0.1}Y_{0.9}O_x$	16.2	18.7	4.8	39.7
$5Ni/Zr_{0.1}Y_{0.9}O_x$	16.0	15.1	4.6	35.7
$5Ni/Al_{0.1}Y_{0.9}O_x$	15.1	15.0	4.8	34.9

2.11. Probing the Reaction Intermediates with In Situ DRIFTS

To explore the possible intermediate species in the DRM reaction, in situ DRIFTS experiments are performed on the reduced $5Ni/Ce_{0.1}Y_{0.9}O_x$ catalyst in a CH_4/CO_2 feed, which simulates the kinetic reaction atmosphere. In Figure 11A, at lower temperatures, the typical adsorbed species on the catalyst surface are bicarbonate (1649 cm^{-1}, 1438 cm^{-1}) [47]. With the reaction temperature increase, the bicarbonate peak gradually weakens. When the temperature rises to 200 °C, the bicarbonate species almost disappears. At the same time, new peaks appear at 1376 cm^{-1} and 1603 cm^{-1}, which are assigned to formate (HCOO*) species [48,49]. This implies that bicarbonate is gradually consumed during the reaction and could be an active intermediate species in the DRM reaction. The CO peak is clearly observed when the temperature is increased to 400 °C, and the peak of formate species reaches maximum intensity. Subsequently, as the temperature increases, the formate and CO peaks weaken at the same time, and the changes in the two with temperature are the same [50,51]. Hence, formate could be an active intermediate species that can be converted into CO. For the bidentate carbonate species at 1458 cm^{-1}, although its peak also gradually increases at the higher-temperature region (200–500 °C), the variation trend of this species with temperature is inconsistent with that of CO species. This testifies that the bidentate carbonate species does not participate in the reaction.

In order to illustrate more intuitively that the bidentate carbonate is not the active intermediates, another series of experiments are conducted by introducing only CO_2 gas onto the reduced $5Ni/Ce_{0.1}Y_{0.9}O_x$ catalyst. As shown in Figure 11B, under the same conditions with only CO_2 gas, the peak of bidentate carbonate species gradually increases in the higher-temperature range, but the bicarbonate species is converted into formate species gradually, until it disappears. This affirms that the bidentate carbonates are easily formed at higher temperatures and might not be active intermediate species.
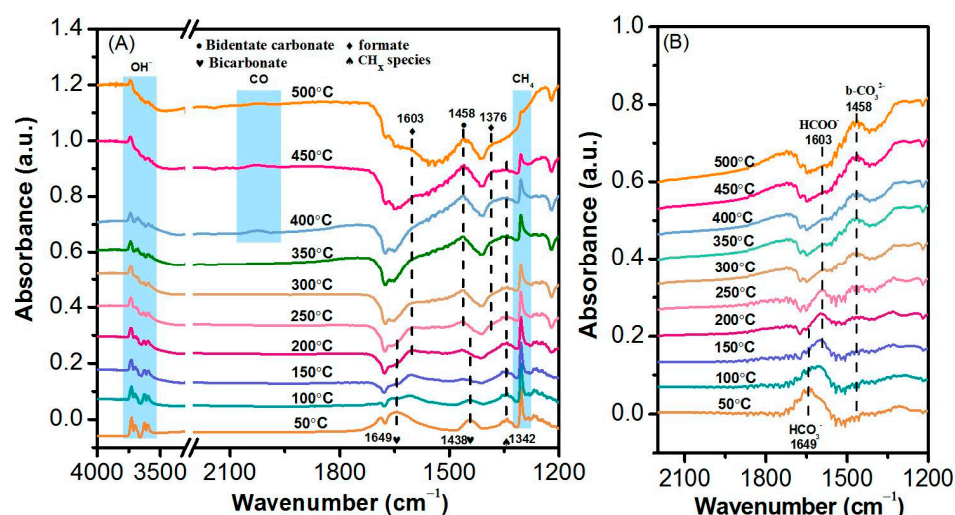

Figure 11. (**A**) In situ DRIFTS spectra of $CH_4 + CO_2$ reaction on the reduced $5Ni/Ce_{0.1}Y_{0.9}O_x$ catalyst at different temperatures, (**B**) In situ DRIFTS spectra of CO_2 reaction on the reduced $5Ni/Ce_{0.1}Y_{0.9}O_x$ catalyst at different temperatures.

Figure S4 compares the in situ DRIFTS spectra of $5Ni/Y_2O_3$, $5Ni/Ce_{0.1}Y_{0.9}O_x$, $5Ni/Zr_{0.1}Y_{0.9}O_x$, and $5Ni/Al_{0.1}Y_{0.9}O_x$ catalysts recorded under the same condition of experiments in Figure 11A. By increasing the temperature, it is observed that the evolution of the intermediate species in the DRM reaction is basically the same, and the bicarbonate gradually converts into formate, indicating that the same DRM mechanism occurs on all the catalysts either unmodified or modified. However, the consumption rates of formate on the three modified catalysts are faster than that on the unmodified $5Ni/Y_2O_3$, especially on the Ce- and Al-promoted catalysts. This indicates that the doping of the secondary metal cations can improve the DRM activity of the modified catalysts, through accelerating the conversion of formate species.

3. Materials and Methods

3.1. Catalyst Preparation

The Y_2O_3 supports unmodified or modified with Ce, Zr, and Al were prepared by a co-precipitation method. Taking the preparation of the $Ce_{0.1}Y_{0.9}O_x$ support as an example here, the calculated amounts of $Y(NO_3)_3 \cdot 5H_2O$ (AR) and $Ce(NO_3)_3 \cdot 6H_2O$ (AR) were dissolved in 10 mL of DDI water at the molar ratio of Y/Ce = 9:1, and stirred at room temperature until the solution was clear. A certain amount of aqueous ammonia (25–28%) was slowly dripped into the solution to adjust its pH around 9.5. After aging for 3–5 h, the solution turned into a white turbid liquid, which was then centrifuged, vacuum-filtered, and washed with DDI water until the TDS of the filtrate was below 20. The filtered solid was dried overnight at 110 °C, then grounded and calcined at 750 °C in a muffle furnace in air for 3 h to obtain the final white product. The synthesis of Zr- or Al-modified Y_2O_3 supports was similar to that of $Ce_{0.1}Y_{0.9}O_x$ except that the solution mixture of $Zr(NO_3)_4 \cdot 5H_2O$ (AR) or $Al(NO_3)_3 \cdot 9H_2O$ (AR) with $Y(NO_3)_3 \cdot 5H_2O$ was used. The prepared supports were denoted as $Ce_{0.1}Y_{0.9}O_x$, $Zr_{0.1}Y_{0.9}O_x$, and $Al_{0.1}Y_{0.9}O_x$, respectively.

The unmodified or modified 5 wt% Ni/Y_2O_3 catalysts were prepared by the impregnation method. First, a certain amount of a desired support was added into a suitable amount of $Ni(NO_3)_2 \cdot 6H_2O$ (>98.0%). After stirring at room temperature for 3 h, the catalyst was dried in a water bath at 80 °C and further dried overnight at 110 °C, which was finally calcined in an air atmosphere for 4 h at 650 °C. The unmodified catalyst was labeled as $5Ni/Y_2O_3$, and the modified samples were labeled as $5Ni/Ce_{0.1}Y_{0.9}O_x$, $5Ni/Zr_{0.1}Y_{0.9}O_x$, and $5Ni/Al_{0.1}Y_{0.9}O_x$, accordingly.

3.2. Activity Evaluation

The DRM reaction performance was evaluated in a quartz tube fix bed reactor having a 6 mm diameter at 1 atm. The average sizes of the used catalysts were 0.3–0.4 mm. The catalysts were first reduced in a 30 mL·min⁻¹ 10% H_2/Ar flow at 600 °C for 2 h, then switched to a gas with a CH_4 and CO_2 ratio of 1:1 (the total flow rate of the mixed gas was 30 mL·min⁻¹). The activity tests of the catalysts were carried out in the temperature range of 600–800 °C under the condition of a gas hour space velocity (GHSV) of 18,000 mL·g⁻¹·h⁻¹. The products were analyzed by an online GC7900 with a TDX-01 column and a TCD in a 99.999% Ar carrier gas flow to monitor the concentrations of H_2, CO, CO_2, and CH_4.

The CH_4 conversion is calculated by:

$$X_{CH_4} = \frac{n_{CH_4,in} - n_{CH_4,out}}{n_{CH_4,in}} \times 100\%$$

The CO_2 conversion is calculated by:

$$X_{CO_2} = \frac{n_{CO_2,in} - n_{CO_2,out}}{n_{CO_2,in}} \times 100\%$$

The H_2 selectivity is calculated by:

$$S_{H_2} = \frac{n_{H_2,out}}{2 \times \left(n_{CH_4,in} - n_{CH_4,out}\right)} \times 100\%$$

The H_2 yield is calculated by:

$$Y_{H_2} = X_{CH_4} \times S_{H_2} = \frac{n_{H_2,out}}{2 \times n_{CH_4,in}} \times 100\%$$

H_2/CO ratio is calculated by:

$$\frac{H_2}{CO} = \frac{n_{H_2,out}}{n_{CO,out}}$$

It is noted that n_{CH_4}, n_{CO_2}, n_{H_2}, and n_{CO} in the equations represent the quantity of a corresponding component calculated from multiplying its integrated area with its response factor on the basis of carbon balance.

By varying the catalyst dosage, the CH_4 conversion below 10% on all catalysts was collected over the temperature range of 450–500 °C to obtain differential reaction rates in the kinetic system.

Rw is the CH_4 conversion rate (mol·g⁻¹·s⁻¹) and the formula is as follows:

$$Rw = \frac{RF \times V\% \times X_{CH_4}}{m_{cat} \times 22.4} \left(mmol \cdot g^{-1} \cdot s^{-1}\right)$$

The RF is the gas flow rate (mL·min⁻¹), V% is the volume fraction of CH_4 in the reaction gas, X_{CH_4} is the CH_4 conversion rate, and m_{cat} is the catalyst mass.

The dispersion of Ni on the reduced catalyst was determined by H_2-sorption experiment. The turnover frequency (TOF) based on exposed Ni surface active sites for CH_4 conversion was calculated.

$$TOF = \frac{R_w \times M_{Ni}}{D_{Ni} \times X_{Ni}}$$

M_{Ni} is the molar mass of Ni atoms, X_{Ni} is the content of Ni, and D_{Ni} is the degree of dispersion of Ni.

3.3. Catalyst Characterization

The detailed techniques, methods, and procedures for catalyst characterization are listed in the Supplementary Materials.

4. Conclusions

With the purpose to fabricate more efficient catalysts for DRM reaction, Ce-, Zr-, and Al-modified Y_2O_3 supports were prepared by the co-precipitation method to support Ni/NiO. XRD and Raman results have testified that all the three cations can be doped into the lattice of cubic Y_2O_3 to form solid solutions, thus resulting in modified supports with decreased crystallinity and improved surface areas. As a result, the modified catalysts display evidently improved DRM rection performance, including enhanced activity, stability, and coking resistance. To elucidate the reasons leading to the performance improvement, the catalysts were characterized with different techniques.

1. H_2-TPR results have indicated that with the secondary metal doping, the Ni–support interaction is enhanced in comparison with the unmodified $5Ni/Y_2O_3$ catalyst. As a result, the modified catalysts have decreased Ni crystallite sizes with improved Ni dispersion, as demonstrated by XRD, TEM, and H_2 adsorption results, which is important to enhance the activity, stability, and anti-coking ability in the DRM reaction. In addition, all the modified catalysts have improved alkalinity, which is beneficial to activate CO_2 and enhance the activity.

2. O_2-TPD and XPS O 1s analyses have testified that all the modified catalysts possess a richer amount of surface active oxygen species ($O_2^{\delta-}$ and O_2^{-}) than the unmodified $5Ni/Y_2O_3$ catalyst, which obeys the order of $5Ni/Ce_{0.1}Y_{0.9}O_x > 5Ni/Zr_{0.1}Y_{0.9}O_x > 5Ni/Al_{0.1}Y_{0.9}O_x > 5Ni/Y_2O_3$, and is well consistent with the coking-resistance sequence. This indicates that the surface active oxygen species is critical to eliminate carbon depositions.

3. In situ DRIFTS results have confirmed that the addition of the secondary metals can improve the DRM activity of the Ni/Y_2O_3 catalyst by accelerating the conversion of formate intermediate species.

4. Among all the catalysts, $5Ni/Al_{0.1}Y_{0.9}O_x$ owns the highest active Ni surface area, thus showing the best activity. In contrast, $5Ni/Ce_{0.1}Y_{0.9}O_x$ possesses the largest amount of surface alkaline sites and active oxygen species, hence displaying the highest stability and the best anti-coking ability.

Author Contributions: Conceptualization, X.W.; methodology, Z.C.; software, Z.C.; validation, X.W., Z.C. and X.F.; formal analysis, X.W. and Z.C.; investigation, Z.C. and L.M.; resources, X.W.; data curation, Z.C. and L.M.; writing—original draft preparation, Z.C.; writing—review and editing, X.W. and X.F.; visualization, X.W. and Z.C.; supervision, X.W. and X.F.; project administration, X.W., J.X. and X.X.; funding acquisition, X.W., X.X., J.X. and X.X. All authors have read and agreed to the published version of the manuscript.

Data Availability Statement: The additional data are available in the separate Supplementary Materials.

Conflicts of Interest: The authors declare no conflict of interest. The funders had no role in the design of the study; in the collection, analyses, or interpretation of data; in the writing of the manuscript; or in the decision to publish the results.

References

1. Li, Z.; Das, S.; Hongmanorom, P.; Dewangan, N.; Wai, M.H.; Kawi, S. Silica-based micro- and mesoporous catalysts for dry reforming of methane. *Catal. Sci. Technol.* **2018**, *8*, 2763–2778. [CrossRef]
2. Al-Fatesh, A.S.; Abu-Dahrieh, J.K.; Atia, H.; Armbruster, U.; Ibrahim, A.A.; Khan, W.U.; Abasaeed, A.E.; Fakeeha, A.H. Effect of pre-treatment and calcination temperature on Al_2O_3-ZrO_2 supported Ni-Co catalysts for dry reforming of methane. *Int. J. Hydrog. Energy* **2019**, *44*, 21546–21558. [CrossRef]
3. Gopaul, S.G.; Dutta, A. Dry reforming of multiple biogas types for syngas production simulated using Aspen Plus: The use of partial oxidation and hydrogen combustion to achieve thermo-neutrality. *Int. J. Hydrog. Energy* **2015**, *40*, 6307–6318. [CrossRef]
4. Zhang, G.; Liu, J.; Xu, Y.; Sun, Y. A review of CH_4-CO_2 reforming to synthesis gas over Ni-based catalysts in recent years (2010–2017). *Int. J. Hydrog. Energy* **2018**, *43*, 15030–15054. [CrossRef]
5. Motomura, A.; Nakaya, Y.; Sampson, C.; Higo, T.; Torimoto, M.; Tsuneki, H.; Furukawa, S.; Sekine, Y. Synergistic effects of Ni-Fe alloy catalysts on dry reforming of methane at low temperatures in an electric field. *RSC Adv.* **2022**, *12*, 28359–28363. [CrossRef] [PubMed]
6. Yang, B.; Deng, J.; Li, H.; Yan, T.; Zhang, J.; Zhang, D. Coking-resistant dry reforming of methane over Ni/gamma-Al_2O_3 catalysts by rationally steering metal-support interaction. *Iscience* **2021**, *24*, 102747. [CrossRef] [PubMed]
7. Kuehl, S.; Duedder, H.; Girgsdies, F.; Kaehler, K.; Muhler, M.; Behrens, M. Perovskites as Precursors for Ni/La_2O_3 Catalysts in the Dry Reforming of Methane: Synthesis by Constant pH Co-Precipitation, Reduction Mechanism and Effect of Ru-Doping. *Z. Anorg. Allg. Chem.* **2017**, *643*, 1088–1095. [CrossRef]
8. Xu, L.; Liu, W.; Zhang, X.; Tao, L.; Xia, L.; Xu, X.; Song, J.; Zhou, W.; Fang, X.; Wang, X. Ni/La_2O_3 Catalysts for Dry Reforming of Methane: Insights into the Factors Improving the Catalytic Performance. *Chemcatchem* **2019**, *11*, 2887–2899. [CrossRef]
9. Liu, H.; Swirk, K.; Galvez, M.E.; Da Costa, P. Nickel Supported Modified Ceria Zirconia Lanthanum/Praseodymium/Yttrium Oxides Catalysts for Syngas Production through Dry Methane Reforming. In *10th International Conference on Processing and Manufacturing of Advanced Materials Processing, Fabrication, Properties, Applications (THERMEC)*; Cite Sci Paris: Paris, France, 2018; Volume 941, pp. 2214–2219.
10. Sutthiumporn, K.; Kawi, S. Promotional effect of alkaline earth over Ni-La_2O_3 catalyst for CO_2 reforming of CH_4: Role of surface oxygen species on H_2 production and carbon suppression. *Int. J. Hydrog. Energy* **2011**, *36*, 14435–14446. [CrossRef]
11. Fujita, T.; Peng, X.B.; Yamaguchi, A.; Cho, Y.; Zhang, Y.Z.; Higuchi, K.; Yamamoto, Y.; Tokunaga, T.; Arai, S.; Miyauchi, M.; et al. Nanoporous Nickel Composite Catalyst for the Dry Reforming of Methane. *Acs Omega* **2018**, *3*, 16651–16657. [CrossRef]
12. Al-Fatesh, A.S. Promotional effect of Gd over Ni/Y_2O_3 catalyst used in dry reforming of CH_4 for H_2 production. *Int. J. Hydrog. Energy* **2017**, *42*, 18805–18816. [CrossRef]
13. Bahari, M.B.; Setiabudi, H.D.; Nguyen, T.D.; Phuong, P.T.T.; Truong, Q.D.; Jalil, A.A.; Ainirazali, N.; Vo, D.-V.N. Insight into the influence of rare-earth promoter (CeO_2, La_2O_3, Y_2O_3, and Sm_2O_3) addition toward methane dry reforming over Co/mesoporous alumina catalysts. *Chem. Eng. Sci.* **2020**, *228*, 115967. [CrossRef]
14. Wang, Y.; Li, L.; Wang, Y.; Da Costa, P.; Hu, C. Highly Carbon-Resistant Y Doped NiO-ZrO_m Catalysts for Dry Reforming of Methane. *Catalysis* **2019**, *9*, 1055. [CrossRef]
15. Li, X.; Zhao, Z.-J.; Zeng, L.; Zhao, J.; Tian, H.; Chen, S.; Li, K.; Sang, S.; Gong, J. On the role of Ce in CO_2 adsorption and activation over lanthanum species. *Chem. Sci.* **2018**, *9*, 3426–3437. [CrossRef] [PubMed]
16. Jin, B.; Li, S.; Liu, Y.; Liang, X. Engineering metal-oxide interface by depositing ZrO_2 overcoating on Ni/Al_2O_3 for dry reforming of methane. *Chem. Eng. J.* **2022**, *436*, 135195. [CrossRef]
17. Diao, Y.A.; Zhang, X.; Liu, Y.; Chen, B.B.; Wu, G.H.; Shi, C. Plasma-assisted dry reforming of methane over Mo_2C-Ni/Al_2O_3 catalysts: Effects of beta-Mo_2C promoter. *Appl. Catal. B* **2022**, *301*, 120779. [CrossRef]
18. Chen, Y.; Lu, Q.; Ren, Y.; Peng, R.; Zhang, B.; Huang, W.; Zhao, Y.; Zhang, J. Experimental Investigations on Stability Tailoring of Ni-xFe/Mayenite for CO_2-CH_4 Reforming. *J. Combust. Sci. Technol.* **2022**, *28*, 229–238.
19. Liu, H.; He, D. Properties of Ni/Y_2O_3 and its catalytic performance in methane conversion to syngas. *Int. J. Hydrog. Energy* **2011**, *36*, 14447–14454. [CrossRef]
20. Strnisa, F.; Sagar, V.T.; Djinovic, P.; Pintar, A.; Plazl, I. Ni-containing CeO_2 rods for dry reforming of methane: Activity tests and a multiscale lattice Boltzmann model analysis in two model geometries. *Chem. Eng. J.* **2021**, *413*, 127498. [CrossRef]

21. Wang, F.; Cai, W.; Provendier, H.; Schuurman, Y.; Descorme, C.; Mirodatos, C.; Shen, W. Hydrogen production from ethanol steam reforming over Ir/CeO$_2$ catalysts: Enhanced stability by PrO$_x$ promotion. *Int. J. Hydrog. Energy* **2011**, *36*, 13566–13574. [CrossRef]

22. Sharma, N.D.; Singh, J.; Vijay, A.; Samanta, K.; Pandey, S.D. Investigations of anharmonic effects via phonon mode variations in nanocrystalline Dy$_2$O$_3$, Gd$_2$O$_3$ and Y$_2$O$_3$. *J. Raman Spectrosc.* **2017**, *48*, 822–828. [CrossRef]

23. Messaoudi, H.; Thomas, S.; Djaidja, A.; Slyemi, S.; Barama, A. Study of LaxNiOy and LaxNiOy/MgAl2O4 catalysts in dry reforming of methane. *J. CO$_2$ Util.* **2017**, *24*, 40–49. [CrossRef]

24. Fang, X.; Xia, L.; Li, S.; Hong, Z.; Yang, M.; Xu, X.; Xu, J.; Wang, X. Superior 3DOM Y$_2$Zr$_2$O$_7$ supports for Ni to fabricate highly active and selective catalysts for CO$_2$ methanation. *Fuel* **2021**, *293*, 120460. [CrossRef]

25. Xia, L.; Fang, X.; Xu, X.; Liu, Q.; Yang, M.; Xu, J.; Gao, Z.; Wang, X. The promotional effects of plasma treating on Ni/Y$_2$Ti$_2$O$_7$ for steam reforming of methane (SRM): Elucidating the NiO-support interaction and the states of the surface oxygen anions. *Int. J. Hydrog. Energy* **2020**, *45*, 4556–4569. [CrossRef]

26. Silva, R.S.; Cunha, F.; Barrozo, P. Raman spectroscopy of the Al-doping induced structural phase transition in LaCrO$_3$ perovskite. *Solid State Commun.* **2021**, *333*, 114346. [CrossRef]

27. Triyono, D.; Hanifah, U.; Laysandra, H. Structural and optical properties of Mg-substituted LaFeO$_3$ nanoparticles prepared by a sol-gel method. *Results Phys.* **2020**, *16*, 102995. [CrossRef]

28. Xia, Y.; Xie, F.; Wang, L.; Peng, Y.; Ma, D.; Zhu, L.; Zhou, G.; Wang, X.; Zhang, G. Efficient dry reforming of methane with carbon dioxide reaction on Ni@Y$_2$O$_3$ nanofibers anti-carbon deposition catalyst prepared by electrospinning-hydrothermal method. *Int. J. Hydrog. Energy* **2020**, *45*, 31494–31506. [CrossRef]

29. Sun, J.; Luo, D.; Xiao, P.; Jigang, L.; Yu, S. High yield hydrogen production from low CO selectivity ethanol steam reforming over modified Ni/Y$_2$O$_3$ catalysts at low temperature for fuel cell application. *J. Power Sources* **2008**, *184*, 385–391. [CrossRef]

30. Fang, X.; Xia, L.; Peng, L.; Luo, Y.; Xu, J.; Xu, L.; Xu, X.; Liu, W.; Zheng, R.; Wang, X. Ln2Zr2O7 compounds (Ln = La, Pr, Sm, Y) with varied rare earth A sites for low temperature oxidative coupling of methane. *Chin. Chem. Lett.* **2019**, *30*, 1141–1146. [CrossRef]

31. Pereñiguez, R.; Gonzalez-delaCruz, V.M.; Caballero, A.; Holgado, J.P. LaNiO$_3$ as a precursor of Ni/La$_2$O$_3$ for CO$_2$ reforming of CH$_4$: Effect of the presence of an amorphous NiO phase. *Appl. Catal. B* **2012**, *123–124*, 324–332. [CrossRef]

32. Sun, G.B.; Hidajat, K.; Wu, X.S.; Kawi, S. A crucial role of surface oxygen mobility on nanocrystalline Y$_2$O$_3$ support for oxidative steam reforming of ethanol to hydrogen over Ni/Y$_2$O$_3$ catalysts. *Appl. Catal. B* **2008**, *81*, 303–312. [CrossRef]

33. Nurk, G.; Kooser, K.; Urpelainen, S.; Käämbre, T.; Joost, U.; Kodu, M.; Kivi, I.; Kanarbik, R.; Kukk, E.; Lust, E. Near ambient pressure X-ray photoelectron-and impedance spectroscopy study of NiO-Ce$_{0.9}$Gd$_{0.1}$O$_{2-\delta}$ anode reduction using a novel dual-chamber spectroelectrochemical cell. *J. Power Sources* **2018**, *378*, 589–596. [CrossRef]

34. Oemar, U.; Hidajat, K.; Kawi, S. High catalytic stability of Pd-Ni/Y$_2$O$_3$ formed by interfacial Cl for oxy-CO$_2$ reforming of CH$_4$. *Catal. Today* **2017**, *281*, 276–294. [CrossRef]

35. Singha, R.K.; Yadav, A.; Agrawal, A.; Shukla, A.; Adak, S.; Sasaki, T.; Bal, R. Synthesis of highly coke resistant Ni nanoparticles supported MgO/ZnO catalyst for reforming of methane with carbon dioxide. *Appl. Catal. B* **2016**, *191*, 165–178. [CrossRef]

36. Singha, R.K.; Shukla, A.; Yadav, A.; Konathala, L.N.S.; Bal, R. Effect of metal-support interaction on activity and stability of Ni-CeO$_2$ catalyst for partial oxidation of methane. *Appl. Catal. B* **2016**, *202*, 473–488. [CrossRef]

37. Zhang, M.; Zhang, J.; Zhou, Z.; Chen, S.; Zhang, T.; Song, F.; Zhang, Q.; Tsubaki, N.; Tan, Y.; Han, Y. Effects of the surface adsorbed oxygen species tuned by rare-earth metal doping on dry reforming of methane over Ni/ZrO$_2$ catalyst. *Appl. Catal. B* **2019**, *264*, 118522. [CrossRef]

38. Fan, Y.; Miao, C.; Yue, Y.; Hua, W.; Gao, Z. Oxidative coupling of methane over Y$_2$O$_3$ and Sr–Y$_2$O$_3$ nanorods. *React. Kinet. Mech. Catal.* **2021**, *134*, 711–725. [CrossRef]

39. Zeng, R.; Jin, G.; He, D.; Zhang, L.; Chen, D.; Zhang, Y.; Zhu, L.; Mei, Y.; Wu, W.; Luo, Y. Oxygen vacancy promoted CO$_2$ activation over acidic-treated LaCoO$_3$ for dry reforming of propane. *Mater. Today* **2022**, *19*, 100162. [CrossRef]

40. Yang, J.; Hu, S.; Fang, Y.; Hoang, S.; Li, L.; Yang, W.; Liang, Z.; Wu, J.; Hu, J.; Xiao, W.; et al. Oxygen Vacancy Promoted O$_2$ Activation over Perovskite Oxide for Low-Temperature CO Oxidation. *ACS Catal.* **2019**, *11*, 9757–9763. [CrossRef]

41. Fei, Z.; He, S.; Li, L.; Ji, W.; Au, C.-T. Morphology-directed synthesis of Co$_3$O$_4$ nanotubes based on modified Kirkendall effect and its application in CH$_4$ combustion. *Chem. Commun.* **2012**, *48*, 853–855. [CrossRef]

42. Long, R.Q.; Wan, H.L. In situ confocal microprobe Ramanspectroscopy study of CeO$_2$/BaF$_2$ catalyst for theoxidative coupling of methane. *J. Chem. Soc. Faraday Trans.* **1997**, *93*, 355–358. [CrossRef]

43. Xu, J.; Xi, R.; Zhang, Z.; Zhang, Y.; Xu, X.; Fang, X.; Wang, X. Promoting the surface active sites of defect BaSnO$_3$ perovskite with BaBr$_2$ for the oxidative coupling of methane. *Catal. Today* **2020**, *374*, 29–37. [CrossRef]

44. Abd Ghani, N.A.; Azapour, A.; Syed Muhammad, A.F.; Abdullah, B. Dry reforming of methane for hydrogen production over NiCo catalysts: Effect of NbZr promoters. *Int. J. Hydrog. Energy* **2018**, *44*, 20881–20888. [CrossRef]

45. Sun, J.; Wang, Y.; Zou, H.; Guo, X.; Wang, Z.-j. Ni catalysts supported on nanosheet and nanoplate γ-Al$_2$O$_3$ for carbon dioxide methanation. *J. Energy Chem.* **2017**, *29*, 3–7. [CrossRef]

46. Solis-Garcia, A.; Louvier-Hernandez, J.F.; Almendarez-Camarillo, A.; Fierro-Gonzalez, J.C. Participation of surface bicarbonate, formate and methoxy species in the carbon dioxide methanation catalyzed by ZrO$_2$-supported Ni. *Appl. Catal. B* **2017**, *218*, 611–620. [CrossRef]

47. Zhang, S.; Ying, M.; Yu, J.; Zhan, W.; Wang, L.; Guo, Y.; Guo, Y. $Ni_xAl_1O_{2-\delta}$ mesoporous catalysts for dry reforming of methane: The special role of $NiAl_2O_4$ spinel phase and its reaction mechanism. *Appl. Catal. B* **2021**, *291*, 120047. [CrossRef]

48. Cao, T.; You, R.; Zhang, X.; Chen, S.; Li, D.; Zhang, Z.; Huang, W. An in situ DRIFTS mechanistic study of CeO_2-catalyzed acetylene semihydrogenation reaction. *Phys. Chem. Chem. Phys.* **2018**, *20*, 9659–9670. [CrossRef]

49. Lavoie, J.-M. Review on dry reforming of methane, a potentially more environmentally-friendly approach to the increasing natural gas exploitation. *Front. Chem.* **2014**, *2*, 1–17. [CrossRef]

50. Jiang, S.; Lu, Y.; Wang, S.; Zhao, Y.; Ma, X. Insight into the reaction mechanism of CO_2 activation for CH_4 reforming over NiO-MgO: A combination of DRIFTS and DFT study. *Appl. Surf. Sci.* **2017**, *416*, 59–68. [CrossRef]

51. Munera, J.; Irusta, S.; Cornaglia, L.; Lombardo, E.; Vargascesar, D.; Schmal, M. Kinetics and reaction pathway of the CO_2 reforming of methane on Rh supported on lanthanum-based solid. *J. Catal.* **2007**, *245*, 25–34. [CrossRef]